Photoionization cross sections of the aluminumlike Si^+ ion in the region of the $2p$ threshold (94–137 eV)

E. T. Kennedy,[1] J.-P. Mosnier,[1,*] P. Van Kampen,[1] D. Cubaynes,[2,3] S. Guilbaud,[2] C. Blancard,[4] B. M. McLaughlin,[5,6] and J.-M. Bizau[2,3]

[1]*National Centre for Plasma Science and Technology, School of Physical Sciences, Dublin City University, Glasnevin, Dublin 9, Ireland*

[2]*Institut des Sciences Moléculaires d'Orsay, CNRS UMR No. 8214, Université Paris–Sud, Bâtiment 350, F-91405 Orsay, France*

[3]*Synchrotron SOLEIL, L'Orme des Merisiers, Saint-Aubin, BP 48, F-91192 Gif-sur-Yvette, France*

[4]*CEA, DAM, DIF, F-91297 Arpajon, France*

[5]*Centre for Theoretical Atomic, Molecular and Optical Physics, School of Mathematics and Physics, Queen's University Belfast, Belfast BT7 1NN, United Kingdom*

[6]*Institute for Theoretical Atomic and Molecular Physics, Harvard Smithsonian Center for Astrophysics, MS-14, Cambridge, Massachusetts 02138, USA*

(Received 10 September 2014; published 1 December 2014)

We present measurements of the absolute photoionization cross section of the aluminumlike Si^+ ion over the 94–137 eV photon energy range. The measurements were performed using the merged-beam setup on the PLEIADES beamline at the SOLEIL synchrotron radiation facility. Signals produced in the Si^{2+} and Si^{3+} photoionization channels of the $2p$ subshell of the Si^+ ion from both the $1s^22s^22p^63s^23p\,^2P_{1/2,3/2}$ ground levels and the $1s^22s^22p^63s3p^2\,^4P$ metastable levels were observed. Absolute cross sections were determined. Calculations of the $2p$ inner-shell photoionization cross sections were carried out using the multiconfiguration Dirac-Fock and Dirac-Coulomb R-matrix theoretical approaches and are compared with experiment.

DOI: 10.1103/PhysRevA.90.063409 PACS number(s): 32.80.Fb, 32.80.Zb

I. INTRODUCTION

The interaction of photons with atoms or ions is a fundamental process in nature. Laboratory investigations of photoabsorption and photoionization are therefore important in the context of a wide range of modeling and applications, not least because radiative recombination is the inverse process of direct photoionization. For example, reliable cross-section data are required for astrophysical interpretations and modeling of laboratory plasmas.

A useful review [1] of the interplay between laboratory-based research and interpretation of astrophysical observations emphasizes that understanding the cosmos rests firmly on scientific knowledge in atomic, molecular, condensed matter, plasma, nuclear, and particle physics. The importance of photoionization in low stages of ionization in determining the presence of absorption lines in the continuum of distant bright stars is well established [2]. Absorption-line spectroscopy remains a powerful tool to estimate element abundances, in both the nearby and distant universe, with an accuracy limited by the accuracy of the relevant atomic data [3–8]. Astrophysical spectra at high photon energies are recorded by satellites such as the Chandra X-ray Observatory [9].

Investigations of atomic ions can also provide valuable insights into atomic effects in molecules, clusters, condensed matter, and plasmas. Silicon is an important atom in many molecules and a wide range of studies has been carried out, for example, on Si $2p$ excitations in various neutral molecules such as SiH_4 and SiD_4 using photoelectron spectroscopy [10,11]. Reactions of Si^+ ions with various molecular species have been examined [12] as has also the role of silicon and its ions, including Si^+, arising from the central role that silicon plays in plasma and materials processing in the microelectronics industry [13].

As silicon is one of the most abundant cosmic species, silicon ions are particularly important in astrophysics as evidenced by many theoretical and experimental investigations over the past few decades. For example, it was pointed out in [14] that "the Si II spectrum is a typical signature of astrophysical plasmas in the temperature range between 5000 and [20 000 K]" and that "silicon's first ion has strong resonance lines in the ultraviolet spectrum, which have been identified in a broad variety of objects." Collections of experimental and theoretical oscillator strengths for 83 Si^+ multiplets were compared [15] to obtain a critical compilation of values. The role of silicon UV absorption in the atmospheres of early-type stars was investigated in [16]. Photoionization resonances of Si^+ in stellar spectra were compared with calculations using the R-matrix code [14], which provided detailed cross sections for the first 50 levels of Si^+. The calculated cross sections were included in the calculation of the far UV synthetic spectrum of A and late B-type stars and it was noted that the Si II opacity is comparable to the H I opacity at many frequencies. Total recombination rate coefficients for Si^+ were calculated [17] using a new unified treatment for electron-ion recombination. The consequences of inner-shell photoionization followed by Auger decays have been considered in the context of ionization balance for the case of silicon in an interstellar medium undergoing soft-x-ray irradiation [18], while [19] describes the case of isoelectronic aluminum in excited states produced through inner-shell photoionization followed by radiationless transitions.

In the laboratory, the dual laser plasma (DLP) technique allowed photoabsorption data for inner-shell resonances and relative cross sections of different atomic ions to be explored [20]. In the DLP technique the absorbing ionized laser plasma plume is backlit by a hot and dense laser plasma emitting a

*Corresponding author: jean-paul.mosnier@dcu.ie

broadband continuum allowing typically a 20–30 eV spectral range to be captured at once. This is ideal for early exploratory work as it enables the positions of inner-shell resonances to be obtained relatively simply. Knowing the energy positions of the resonances is an advantage for follow-up work at synchrotron or ion beam facilities, which operate in photon energy scanning mode. While the DLP technique is extremely versatile [21], DLP spectra can show distortions due to plasma effects and/or saturation of strong features, so certain assumptions must be made when comparing relative cross-section data with theoretical calculations [22]. The development of dedicated ion sources at synchrotron facilities has overcome these limitations and enables systematic high-resolution investigations, which in several cases uniquely provide absolute photoionization cross-section values [23–26]. The experimental data, while providing valuable information for the interpretation of laboratory and astrophysical plasmas, are important also for testing different theoretical calculations [27,28]. As the individual interparticle interactions are known, atoms and ions are ideal testing grounds for many-body theories. The study of isonuclear or isoelectronic sequences, where the number of electrons or the nuclear charge is systematically changed, has been shown to be a powerful tool in the investigation of trends in physical behavior and the development of associated physical insight [29,30].

Following prior DLP investigations on the isonuclear Si^{2+} [31] and Si^{4+} [32] ions in which photoabsorption spectra were obtained in the inner-shell $2p$ excitation regions, more detailed experiments were later carried out using the synchrotron radiation available at the SuperACO storage ring [33,34]. The present paper reports a synchrotron-based photoionization investigation of the isonuclear singly ionized silicon ion Si^+. This aluminumlike ion provides a particular challenge resulting from its complex spectrum due to its open-shell nature and a high-spectral-resolution facility is required. This was provided by the merged-beam setup at the PLEIADES beamline on the third-generation synchrotron SOLEIL facility [35,36]. Earlier DLP work on Si^+ reported in Refs. [37,38] showed a strong series of resonances in the $2p$ inner-shell excitation region and comparison with the results of multiconfiguration Hartree-Fock calculations allowed some early insights into the dominant configurations responsible for the line strengths. In the current work the use of ion spectrometry combined with synchrotron radiation provides separation of the single- and double-partial-photoionization cross sections producing Si^{2+} and Si^{3+} ions, respectively. The high spectral resolution of the PLEIADES beam line allowed us to study the observed resonances in both channels in considerable detail and furthermore, cross sections, for both resonances and continuum, have been put on an absolute basis. Our results are also important in terms of comparing and benchmarking different theoretical methods, which need to accurately account for the complexities arising from electron correlation effects if they are to provide reliable results.

II. EXPERIMENTAL SETUP AND PROCEDURE

The experiments were performed on the merged-beam setup [35] permanently installed on the PLEIADES beam line at SOLEIL [36]. Si^+ ions were produced in a permanent magnet electron cyclotron resonance ion source (ECRIS) by heating silane gas by a 12.6-GHz radio-frequency wave, with a power less than 10 W. The ions were extracted by applying a 4-kV acceleration voltage to the source and then selected by a first dipole magnet before merging with the monochromatized synchrotron radiation (SR). After the interaction, the ions were charge separated by a second dipole magnet. The parent Si^+ ions were collected in a Faraday cup and the photoions, the ions that have gained one or two charges in the interaction with the photons, were counted using microchannel plates. A low-frequency chopper (typically 0.1 Hz) located at the entrance of the photon beam to the interaction region allowed the subtraction of the counts produced by collisional processes of the parent Si^+ ions with the residual gas in the vacuum chamber or with the slits used to collimate the ion beam. In order to minimize the background counts, a pressure in the 10^{-10}-mbar range was maintained in the interaction chamber.

The SR beam was produced in a permanent magnet Apple II undulator with 80-mm period and monochromatized by a plane grating monochromator. For this work, a high-flux 600-line/mm grating was used, with variable groove depth technology to provide a high spectral purity. The photon flux was determined from the current produced on a calibrated photodiode. The photon energy was determined using a double-ionization gas cell of Samson type [39]. For the calibration, we used the $4d \rightarrow 6p$ transition in Xe gas at 65.110 eV, the $3d \rightarrow 5p$ transition in Kr gas at 91.200 eV, and the $2p \rightarrow 3d$ transition in Ar gas at 244.390 eV [40]. The photon energy was corrected for the Doppler shift resulting from the velocity of the Si^+ ions. Excellent reproducibility of the resonance energies was obtained in different experimental scans. The accuracy for the photon absolute energy determination was between 20 and 30 meV, primarily determined by the accuracy of the rare-gas excitation energies used as references.

With this setup, the photoionization cross sections σ were determined in absolute value from

$$\sigma = \frac{Se^2\eta v q}{I J \varepsilon \int_0^L dz \,/\, \Delta x \Delta y F(z)}, \tag{1}$$

where S is the photoion counting rate measured with microchannel plates of known efficiency ε, e the charge of the electron, I the current produced by the Physikalisch-Technische Bundesanstalt calibrated photodiode of efficiency η, v the velocity of the Si^+ ions having charge $q = 1$, J the current of the Si^+ ion beam measured with the Faraday cup, and $\Delta x \Delta y F(z)$ an effective beam area (z is the propagation axis of the ion and photon beams), with F a two-dimensional form factor determined using three sets of xy scanners placed at each end and in the middle of the interaction region [41]. The interaction region was a tube of length $L = 50$ cm. A -600-V bias was applied to the tube in order to tag the photoions produced inside the tube, these having a different velocity exiting the tube than the photoions produced outside the tube. Table I gives typical values and uncertainties for the parameters involved in Eq. (1), measured for the determination of the single-photoionization cross section at 119.6-eV photon energy. The resulting relative uncertainty for the absolute cross sections was in the 10%–15% range.

TABLE I. Typical values and associated uncertainties for the experimental parameters of Eq. (1).

Parameter	Value	Uncertainty
S	310 Hz	3%
noise	1000 Hz	
v	1.8×10^5 m s^{-1}	<1%
photon flux	6.5×10^{13} s^{-1}	4%
J	73 nA	<1%
ε	0.41	6%
$F(z)$	26	5%
σ	1.79 Mb	11%

In a second mode of acquisition, no voltage was applied to the tube in the interaction region, offering a longer photon ion-beam interaction region and a counting rate roughly multiplied by a factor of 2. In this data acquisition mode, only relative cross sections could be obtained, which were normalized later to the cross sections determined in the absolute mode.

In merged-beam experiments long-lived metastable states produced in the ECRIS can survive to enter the merged-beam region, thus contributing to the observed photoionization signals. The relative populations of ground and excited metastable states therefore need to be taken into account when determining the absolute cross section for the different initial states [41,42].

III. CALCULATIONS

One of the primary drivers of the experimental measurements was to benchmark different theoretical calculations. We therefore carried out a systematic series of calculations using both the multiconfiguration Dirac-Fock (MCDF) and relativistic R -matrix methods within the Dirac-Coulomb approximation. The approaches of the two computational methods are different. The MCDF calculations determine resonance energies and associated oscillator strengths by operating directly on the 12-electron Si^+ ion. The Dirac atomic R -matrix code (DARC) calculations also uses a multiconfiguration approach, but it does so as a first step in order to calculate level energies of the target 11-electron Si^{2+} ion. By comparing the calculated results with known values from the National Institute of Standards and Technology (NIST) tables, the wave functions for the target Si^{2+} atom are iterated, so the ultimate R -matrix scattering results for Si^+ may be improved. Further details on the two contrasting methods are provided in the following sections.

A. Multiconfiguration Dirac-Fock calculations

Multiconfiguration Dirac-Fock calculations were performed based on a full intermediate coupling regime in a jj basis using the code developed by Bruneau [43] in which relaxation of the outer orbitals is taken into account through the use of different functions in the initial and final states. Photoexcitation and photoionization cross sections were calculated for Si^+ ions in the region of the L edge. Only electric dipole transitions were considered using the length form. Photoexcitation and photoionization from the two levels ($^2P_{1/2,3/2}$) of the ground configuration $1s^22s^22p^63s^23p$ and photoexcitation from metastable levels ($^4P_{1/2,3/2,5/2}$) of the configuration $1s^22s^22p^63s3p^2$ were considered. Photoexcitation and photoionization were calculated separately. Multiple orbitals were used in order to describe the correlation and relaxation effects. Wave functions were calculated minimizing the Slater transition state. Concerning photoexcitation processes, each transition was dressed by a Lorenztian profile with a full width half maximum (FWHM) equal to 30 meV. Photoexcitation cross-section calculations were carried out using the following configurations: the initial configurations [Ne] $3s^23p$, $3p^3$, $3p3d^2$, $3s3p^2$, $3p^23d$, $3s^23d$, and $3s3d^2$ and the final configurations [Be,$2p^5$] $3s^23p3d$, $3s3p^3$, $3p^33d$, $3s3p3d^2$, $3p3d^3$, $3s^23p^2$, $3s3p^23d$, $3s^23d^2$, $3p^23d^2$, $3s3d^3$, and $3s^23pnl$ (with $n = 4,5,6$ and $l = 0,1,2$).

Radial functions of $2p$ and $n = 3$ orbitals were not the same for initial and final configurations. Due to numerical instabilities, the configuration [Ne] $3s3p3d$ was excluded from the initial configuration list. The photoionization cross-section calculations were carried through using the [Ne] $3s^23p$ and [Be,$2p^5$] $3s^23p$ configurations.

B. The R -matrix method

Calculations used an efficient parallel version [44] of the suite of codes in [45–47], which was developed [48–51] to address the challenge of electron and photon interactions with atomic systems catering to hundreds of levels and thousands of scattering channels. Recent modifications to the DARC [48–50] allowed high-quality photoionization cross-section calculations to be made on heavy complex systems of prime interest to astrophysics and plasma applications [48,49,51]. Photoionization cross sections for the complex Si^+ ion were calculated for the ground $3s^23p\,^2P^o_{1/2}$ and excited $3s^23p\,^2P^o_{3/2}$ levels. The atomic structure calculations (for the Si^{2+} target ion) were carried out using the GRASP multiconfiguration code [52–54]. The inclusion of target fine structure through the Dirac equation and jj coupling involves a substantial computational commitment [47]. We have used a model, which incorporated 481 levels of the Si^{2+} ion, originating from the following 13 configurations: $2p^63s^2$, $2p^63s3p$, $2p^63s3d$, $2p^63p3d$, $2p^63p^2$, $2p^63d^2$, $2p^53s^23p$, $2p^53s^23d$, $2p^53s3p3d$, $2p^53s3p^2$, $2p^53s3d^2$, $2p^43s^23p^2$, and $2p^43s^23d^2$.

An R -matrix boundary radius of 12.03 bohr radii was sufficient to envelop the radial extent of all the $n = 3$ atomic orbitals of the residual Si^{2+} ion. A basis of 16-continuum orbitals was sufficient to span the incident experimental photon energy range from threshold up to 150 eV. Since dipole selection rules apply, total ground-state photoionization required only the bound-free dipole matrices $J^\pi = 1/2^o \rightarrow J^\pi = 1/2^e,3/2^e$. For the excited $^2P^o_{3/2}$ state, $J^\pi = 3/2^o \rightarrow J^\pi = 1/2^e,3/2^e,5/2^e$ were necessary. In the case of the $^4P_{1/2,3/2,5/2}$ metastable states, we require the bound-free dipole matrices $J^\pi = 1/2^e \rightarrow J^\pi = 1/2^o,3/2^o$; $J^\pi = 3/2^e \rightarrow J^\pi = 1/2^o,3/2^o,5/2^o$; and $J^\pi = 5/2^e \rightarrow J^\pi = 3/2^o,5/2^o$.

For both levels of the ground-state configuration, the outer-region electron-ion collision problem was solved (in

the resonance region below and between all thresholds) using a suitably chosen fine energy mesh of 1.5×10^{-8} Ry ($\sim$0.2 μeV) to fully resolve all the extremely narrow resonance structures in the appropriate photoionization cross sections. The jj -coupled Hamiltonian diagonal matrices for the Si^{2+} target atom were adjusted so that the theoretical term energies matched the recommended experimental values of NIST, where available [55]. We note that this energy adjustment provided better positioning of certain resonances relative to all thresholds included in the final Si^{+} calculation.

IV. ANALYSES AND COMPARISONS WITH THEORY

Figure 1 presents the cross-section variations for the production of doubly (single-ionization channel) and triply (double-ionization channel) ionized ions, upon the interaction of synchrotron photons with a merged Si^{+} ion beam, measured over the full energy range of 94–137 eV covered in this work. The calculated energy bandpass (BP) values at the photon energies of 95, 105, 115, and 121 eV are 60, 70, 90, and 107 meV, respectively.

The main observed features in Fig. 1 are found in three distinct photon energy regions: (i) a number of weak resonances near 95 eV, which are readily identified as due to photoionization of Si^{+} initially in ^4P metastable states above the ground state, (ii) complex patterns of strong and weak resonances in the single- and double-ionization channels between 108 and $\sim$119 eV, respectively, due to various ionization processes following the excitation of a $2p$ -subshell electron, and (iii) the onset, just above a threshold near 119 eV, of an almost constant continuum in the double-ionization channel, arising from ionization processes following the initial ionization of a $2p$ -subshell electron. These various contributions to the total cross section are analyzed separately below, in their corresponding photon energy ranges, in the light of the atomic calculations presented in the previous sections. To help in understanding these analyses, the energy-level structure of the Si^{+} ion showing relevant valence and inner thresholds is depicted in Fig. 2. Some of the levels in this figure are inferred from previous inner-shell photoabsorption measurements and tabulated optical levels [55].

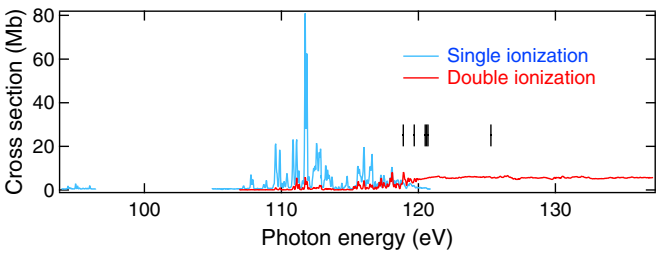

FIG. 1. (Color online) Variation of the photoionization (PI) cross sections of the Si^{+} ion measured for the full energy range 94–137 eV covered in this work. The blue (light gray) and red (dark gray) curves are the single and double PI, respectively. The energy of the various $2p$ ionization thresholds is indicated by vertical bars. The resonances near 95 eV photon energy are shown in greater detail in Fig. 3.

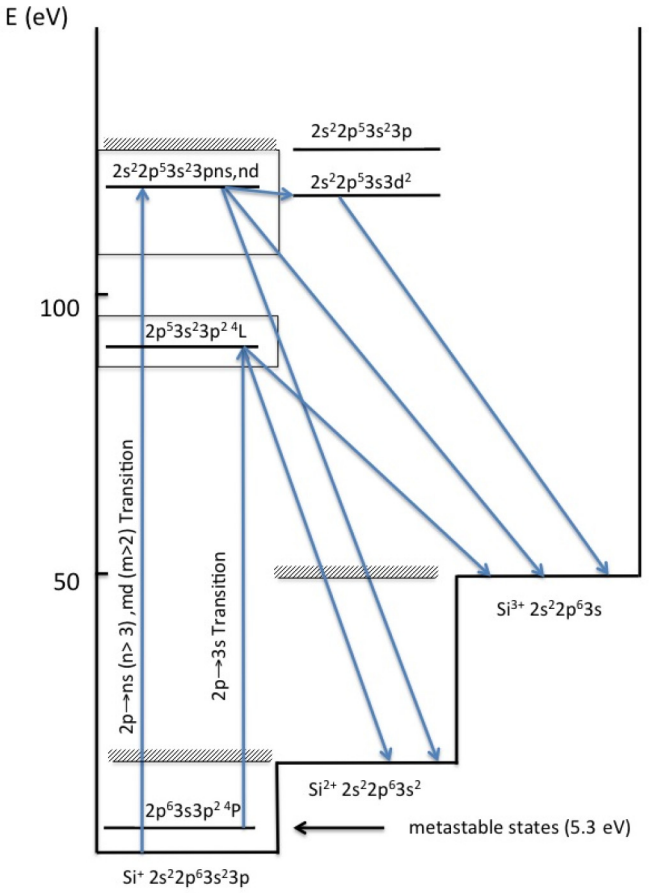

FIG. 2. (Color online) Schematic energy-level diagram showing relevant excitation energies and ionization thresholds.

A. Contribution of metastable states to the cross sections ($\sim$95 eV)

As mentioned in Sec. II, metastable Si^{+} ions, if sufficiently long lived, travel to the photon-ion interaction region, thus contributing to the measured total cross sections. It is therefore important to estimate the metastable relative population in order to allow meaningful comparisons between measured and theoretical cross sections. Transitions arising from Si^{+} metastable states have been observed previously in a DLP photoabsorption experiment, in the spectral region around 95 eV [37]. The observed discrete resonances are due to the valence-excited $2p^6 3s 3p^2\, ^4P_{1/2,3/2,5/2}$ metastable levels, which lie $\sim$5.3 eV above the ground state and can be photoexcited via $2p \rightarrow 3s$ inner-shell transitions to $2p^5 3s^2 3p^2\, ^{4,2}L$ states. The latter can decay via autoionization and produce a Si^{2+} ion signal (single-ionization channel). In Fig. 3 we show the recorded photoionization cross-sectional measurements in this region, together with the corresponding theoretical MCDF simulation (Sec. III A), in the top and middle panels of Fig. 3, respectively, while the numerical details of the corresponding MCDF atomic data are shown in Table II. The experimental cross sections, as a function of photon energy, were determined with a 60-meV bandpass in both relative and absolute modes shown by a solid blue (light gray) line and red (dark gray) data points, respectively. The resonance labels (capital letters) in Fig. 3 refer to the detailed transitions of Table II. The synthetic

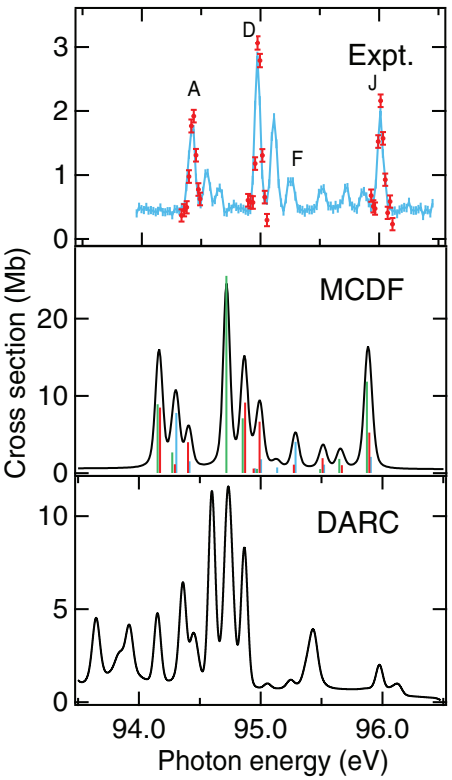

FIG. 3. (Color online) Single-PI cross sections of the Si^+ ion in the $3s3p^2\,{}^4P_{1/2,3/2,5/2}$ metastable levels in the 93.5–96.5 photon energy range. In the top panel the light blue (light gray) points with statistical error bars are the experimental cross sections measured in the relative mode with a 60-meV bandpass. The red (dark gray) points are the cross sections measured in the absolute mode; for the absolute measurements the error bar represents the total uncertainty. The labeling (A, D, F, and J) of the lines refers to Table II. The middle panel shows the MCDF theoretical cross sections (black curve). The heights of the vertical sticks give the relative contribution of the three initial levels with $J = 1/2$, $3/2$, and $5/2$, shown in blue (light gray), red (dark gray), and green (gray), respectively. The bottom panel shows the DARC theoretical cross sections. Both theoretical cross sections have been reconstructed by convolving with a Gaussian profile of 60-meV FWHM (see the text) and assuming a statistical population of the $J = 1/2$, $3/2$, and $5/2$ levels.

cross-section spectrum (middle panel) was constructed from the theoretical MCDF oscillator strengths of the transitions originating in the three initial levels $^4P_{1/2,3/2,5/2}$, assuming a statistical population between the levels, and then convolved with a normalized Gaussian function of 60-meV FWHM.

From Fig. 3 and Table II we see that the agreement between the measured and calculated MCDF resonance energies is within 0.3 eV and satisfactory in terms of relative resonance strengths, allowing straightforward spectroscopic assignments. The results for the DARC numerical approximation are in the bottom panel of Fig. 3, again convoluted with a 60-meV bandpass and also assuming a statistical weighting of the initial levels. The agreement with experiment is not as good in this case for the relative resonance strengths and for this reason we have used the MCDF simulations in estimating the metastable fraction. Such a procedure has also been frequently used in similar works [33]. The integrated cross sections of the resonances are compared between experiment (Fig. 3, top panel) and theory (Fig. 3, middle panel) after subtracting the underlying ground state Si^+ continuum cross section (about 0.3 Mb). The respective integrated cross sections are 1.6 Mb eV from experiment and 16.4 Mb eV from the MCDF calculations. The ratio implies that the Si^+ beam contained a metastable fraction of the order of 10%. This estimation of the metastable fraction, while model dependent, is sufficiently accurate for our purposes. We show later that the role of the relatively minor metastable fraction in determining the cross sections at higher energies is not significant. The theoretical cross sections presented in Secs. IV B and IV C are appropriately scaled to take into account the 90% ground and 10% metastable fractions, unless otherwise stated.

B. Photoionization cross sections between 104 and ∼120 eV

The top and bottom panels of Fig. 4 show the measured variations of the relative (solid line) and absolute (data points with an error bar) single and double Si^+ photoionization cross sections, respectively, as a function of photon energy in the 104–120 eV range. The resonances are uniquely labeled with numbers, also used in Table III (104–112 eV) and Table V (112–120 eV), respectively.

In this energy range, the absorbed photon from the ground levels $2p^6 3s^2 3p\,{}^2P^o$ produces inner-shell ($2p$) excited states that lie below the $2p$ ionization thresholds (see Fig. 2). The $2p^6 3s^2 3p\,{}^2P^o_{3/2}$ level lies 0.0365 eV above the $2p^6 3s^2 3p\,{}^2P^o_{1/2}$ ground-state level and the fine-structure details from each state in the measured cross sections are not resolved. Statistical distribution among the fine-structure levels of the ground configuration is assumed. The $2p$ thresholds, i.e., the Si^{2+} energy levels based on the $2p^5 3s^2 3p$ configuration, were calculated in Ref. [38] from literature data by adding the energy of measured photoabsorption transitions in Si^{2+} [56] to the tabulated ionization energy of Si^+ (16.34 eV) and the known excitation energy of the $2p^6 3s 3p\,{}^3P$ state (6.54 eV) in Si^{2+}. The threshold energies, ignoring fine structure, thus obtained are 118.9 eV (^3S), 119.7 eV (^3D), 120.5 eV (^1P), 120.6 eV (^1D), ∼120.7 eV (^3P), and 125.3 eV (^1S) and are illustrated by vertical bars in Fig. 1. Similar calculations in isoelectronic aluminum find the energies of the $2p^5 3s^2 3p$ states in Al^+ predicted in [56] within a 0.02-eV agreement with the measured values from more recent photoelectron data in atomic aluminum by Jankala *et al.* [57]. This gives confidence in the present values for the Si^+ $2p$ thresholds.

The $2p$ excited resonances are degenerate with the single- and double-ionization continua (see Fig. 2) into which they autoionize (resonant Auger decay), via Coulomb or spin-orbit interactions, by the ejection of one or two electrons (shake-off process). The importance of such processes for aluminum, isoelectronic to Si^+, has been discussed by Kochur *et al.* [19]. Sequential ionization via intermediate Si^{2+} levels can also take place. The doubly (Si^{2+}) and triply (Si^{3+}) charged ions are measured as the final products of the possible decays of the $2p$ excited inner-shell resonances. The experimental variations of the total cross section, i.e., the sum of the single- and double-ionization signals, are displayed in Fig. 5 (top panel) as a function of photon energy in the 105–120 eV range. These can be directly compared with the (see Sec. IV A)

TABLE II. Measured energy position and oscillator strength (f value), spectral term assignment ($2p^6 3s 3p^2\,{}^4P_J \rightarrow 2p^5 3s^2 3p^2\,{}^4L_{J'}$), and theoretical MCDF energy of resonances in the single-photoionization cross-section of Si^+ around 95 eV photon energy. The relative energy uncertainties in meV are shown in parentheses in column 2. The uncertainty on the f value does not include the contribution of the systematic uncertainties.

Resonance label	Measured energy (eV)	Measured f value (% error)	MCDF energy (eV)	Initial J	Final $^{2,4}L_{J'}$
A	94.422	$8.6 \times 10^{-3}(22)$	94.153	5/2	$^4P_{5/2}$
			94.173	3/2	$^4P_{5/2}$
B	94.548(4)	$3.7 \times 10^{-3}(27)$	94.308	1/2	$^4P_{3/2}$
C	94.650(5)	$1.9 \times 10^{-3}(38)$	94.403	3/2	$^4P_{1/2}$
D	94.975(2)	$1.3 \times 10^{-2}(21)$	94.718	5/2	$^4D_{7/2}$
E	95.113(2)	$8.9 \times 10^{-3}(20)$	94.852	5/2	$^4D_{5/2}$
			94.872	3/2	$^4D_{5/2}$
F	95.256(4)	$3.3 \times 10^{-3}(27)$	94.990	3/2	$^4D_{3/2}$
G	95.521(5)	$2.7 \times 10^{-3}(32)$	95.286	1/2	$^4D_{1/2}$
H	95.721(6)	$2.2 \times 10^{-3}(34)$	95.508	3/2	$^2D_{3/2}$
			95.521	1/2	$^2D_{3/2}$
I	95.868(6)	$1.9 \times 10^{-3}(37)$	95.646	5/2	$^2D_{5/2}$
			95.666	3/2	$^2D_{5/2}$
J	96.010(2)	$8.7 \times 10^{-3}(22)$	95.871	5/2	$^4S_{3/2}$
			95.892	3/2	$^4S_{3/2}$

MCDF and DARC theoretical calculations, shown in the middle and bottom panels of Fig. 5, respectively. To account for the experimental broadening in this energy region and thus provide better comparisons between experiment and theories, the calculated cross sections were convolved with a normalized Gaussian profile of 80-meV FWHM. The MCDF simulation shows the relative contributions of the two $J = 1/2, 3/2$ ground levels to the cross sections in the form of stick diagrams with different colors and includes the ^4P metastable contributions to the cross sections in the 108–120 eV region.

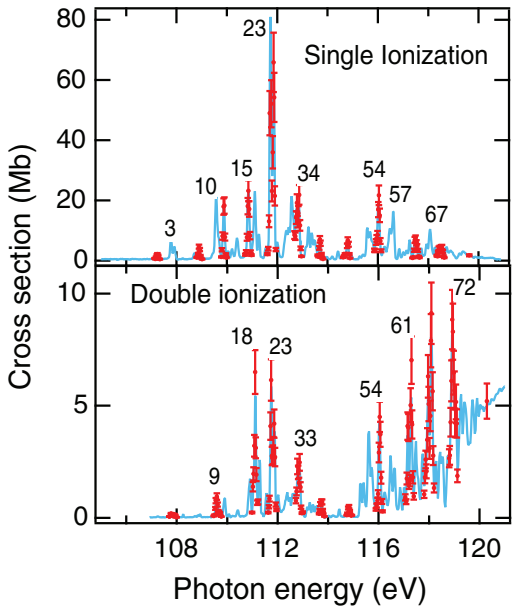

FIG. 4. (Color online) Experimental single (top) and double (bottom) PI cross sections measured with 80-meV BP in the relative and absolute modes shown by blue (light gray) curves and red (dark gray) points, respectively. The numbering of the lines refers to Tables III and V.

The bottom panel of Fig. 5 shows the results of the DARC ground-state calculations for the 105–120 eV region. The calculated cross section has been scaled by the factor 0.9 to take account of the 90% ground-state population, but the relatively small contributions of the metastables were not included. Reasonable agreement is seen for both calculations with the experimental data for the overall shape of the cross section variation as a function of energy.

To illustrate the relative strengths of the ground-state and metastable contributions to the overall cross section, the various contributions to the middle panel of Fig. 5 are detailed in Fig. 6. The MCDF calculated inner-shell excitation resonances in the cross section from the ^2P ground and ^4P metastable levels are shown separately in the top and middle panels of Fig. 6, respectively, whereas the bottom panel of Fig. 6 shows the 90% (^2P) + 10% (^4P) weighted sum of these contributions. Figure 6 shows that the contribution of the ^4P metastables to the overall cross section is negligible below about 111 eV and quite small at higher energies.

The measured energy positions, oscillator strengths, and single- to double-ionization signals strength ratios are presented in Table III for all the resonances measured in the 107–112 eV range; this comprises the low-energy region up to the most intense resonances in the spectrum lying just short of 112 eV. We discuss this part of the spectrum first. The oscillator strengths (f values) are determined from the integrated intensity of Voigt profiles computer fitted to the measured resonance profiles. From Table III and Fig. 5 we see that the discrete resonances in the 107–112 eV region largely dominate the cross-section spectrum below the $2p$ threshold. These correspond to the resonant Auger decay of singly excited and doubly excited states belonging to the even-parity $2p^5 3s^2 3pnd$, $2p^5 3s^2 3p(n+1)s$, and $2p^5 3s 3p^2 np (n = 3)$ configurations, respectively. These configurations contain at least three open electron subshells and thus result in a large number of possible final photoexcited LSJ states due to the many possible intermediate couplings. For example,

TABLE III. Measured energy position, oscillator strength (f value), and single- to double-ionization ratio, spectral assignments, and theoretical MCDF energy of $2p$ -subshell excited resonances in the single- and double-photoionization cross sections of Si^+ in the 107–112 eV photon energy range. The relative energy uncertainties in meV are shown in parentheses in column 2. The uncertainty on the f value does not include the contribution of the systematic uncertainties.

Resonance label	Measured energy (eV)	Measured f value (% error)	Measured Si^{2+}/Si^{3+} ratio	Initial level	Final level	MCDF energy (eV)
1	107.238	1.56×10^{-3}(14)	0.97/0.03	$^2P_{1/2}$	$2p^5 3s 3p^3\ ^4D_{1/2}$	105.07
2	107.630(8)	1.02×10^{-5}(52)	0.00/1.00			
3	107.780(2)	6.34×10^{-3}(13)	0.98/0.02	$^2P_{3/2}$	$2p^5 3s 3p^3\ ^2P_{3/2}$	105.77
4	107.914(2)	3.98×10^{-3}(14)	0.97/0.03	$^2P_{1/2}$	$2p^5 3s 3p^3\ ^2P_{1/2}$	105.89
5	108.252(7)	2.25×10^{-4}(30)	0.72/0.28			
6	108.716(2)	2.32×10^{-3}(14)	0.98/0.02	$^2P_{3/2}$	$2p^5 3s 3d^3\ ^2D_{5/2}$	106.68
7	108.904(2)	3.85×10^{-3}(14)	0.97/0.03	$^2P_{3/2}$	$2p^5 3s 3p^2 3d\ ^2D_{3/2}$	106.80
8	109.431(3)	9.73×10^{-4}(19)	1.00/0.00	$^2P_{3/2}$	$2p^5 3s 3p^3\ ^2D_{5/2}$	107.47
				$^2P_{1/2}$	$2p^5 3s 3p^3\ ^2D_{3/2}$	107.53
9	109.574(2)	2.51×10^{-2}(13)	0.95/0.05	$^2P_{3/2}$	$2p^5 3s^2 3p 3d\ ^2P_{1/2}$	107.62
				$^2P_{1/2}$	$2p^5 3s^2 3p 3d\ ^2P_{1/2}$	107.65
10	109.680(2)	5.14×10^{-3}(14)	0.97/0.03	$^2P_{3/2}$	$2p^5 3s 3p^3\ ^2P_{3/2}$	107.78
				$^2P_{1/2}$	$2p^5 3s 3p^3\ ^2P_{3/2}$	107.81
11	109.881(2)	1.79×10^{-2}(15)	0.95/0.05	$^2P_{3/2}$	$2p^5 3s^2 3p 3d\ ^2P_{3/2}$	107.97
12	110.053(2)	2.18×10^{-3}(15)	0.95/0.05			
13	110.206(2)	2.85×10^{-3}(14)	1.00/0.00			
14	110.407(2)	9.30×10^{-3}(22)	0.97/0.03			
15	110.845(2)	2.03×10^{-2}(33)	0.92/0.08	$^2P_{3/2}$	$2p^5 3s^2 3p 3d\ ^2D_{5/2}$	108.82
16	110.885(6)	6.79×10^{-3}(41)	0.91/0.09			
17	111.037(5)	2.95×10^{-3}(57)	0.57/0.43			
18	111.110(3)	2.64×10^{-2}(22)	0.87/0.13	$^2P_{3/2}$	$2p^5 3s 3p^3\ ^2S_{1/2}$	109.23
				$^2P_{1/2}$	$2p^5 3s 3p^3\ ^2S_{1/2}$	109.26
19	111.163(21)	2.09×10^{-3}(65)	0.62/0.38			
20	111.272(2)	8.46×10^{-3}(13)	0.77/0.23	$^2P_{3/2}$	$2p^5 3s^2 3p 4s\ ^2S_{1/2}$	109.48
				$^2P_{1/2}$	$2p^5 3s^2 3p 4s\ ^2S_{1/2}$	109.51
21	111.399(5)	3.92×10^{-4}(34)	0.89/0.11			
22	111.555(2)	4.94×10^{-3}(13)	0.85/0.15	$^2P_{3/2}$	$2p^5 3s^2 3p 4s\ ^2D_{5/2}$	110.32
23	111.735(2)	7.09×10^{-2}(12)	0.93/0.07	$^2P_{3/2}$	$2p^5 3s^2 3p 3d\ ^2D_{5/2}$	110.505
24	111.810(11)	4.76×10^{-3}(38)	0.77/0.23			
25	111.857(7)	4.91×10^{-2}(13)	0.96/0.04	$^2P_{1/2}$	$2p^5 3s^2 3p 3d\ ^2D_{3/2}$	110.63
26	112.006(2)	6.38×10^{-3}(13)	0.89/0.11	$^2P_{3/2}$	$2p^5 3s^2 3p 4s\ ^2D_{3/2}$	110.80
				$^2P_{1/2}$	$2p^5 3s^2 3p 4s\ ^2D_{3/2}$	110.83

the even-parity configuration $2p^5 3s^2 3pnd$ configuration will produce $[2p^5(^2P)(3s^2 3pnd\,^1S,^1P,^1D,^1F)]^2S,^2P,^2D,^2F,^2G$ and $[2p^5(^2P)(3s^2 3pnd\,^3S,^3P,^3D,^3F)]^{2,4}S,^{2,4}P,^{2,4}D,^{2,4}F,^{2,4}G$ terms with possible $1/2 \leqslant J \leqslant 11/2$ values. The sheer complexity of the resulting spectrum provides a severe challenge to theoretical models. The situation becomes even more complex with an increasing spectral density of resonances for increasing nl values at higher energies. Many of the states can autoionize by Coulomb interaction into the underlying $(2p^6 3s^2 \varepsilon d)\ ^2D^e_{3/2,\,5/2}$ and $(2p^6 3s^2 \varepsilon s)\ ^2S^e_{1/2}$ continua. According to LS -coupling selection rules, a larger number of these LSJ states could Auger decay via spin-orbit interactions and thus also contribute to the observed spectra as more continua are open as possible final states. The DLP absorption data previously measured [38] can be compared directly with the top panel spectrum of Fig. 5. Generally good agreement is observed between the two works in terms of resonance positions (within 0.09 eV) and their respective overall distribution of intensities, although saturation effects are clearly seen in the DLP data. The energy differences are marginally outside the combined uncertainties of the two measurements. For the present experiments the relative energy uncertainties are much smaller than the absolute energy uncertainties and are indicated in parentheses in the relevant tables, i.e., Tables II, III, and V.

Extensive discussions are found in [38] on the difficulties associated with unique resonance labeling and oscillator strengths distributions based on the $2p$ inner-shell excited configurations due to strong configuration-interaction (CI) effects in both the valence and excited configurations (see also [57] for similar discussions in isolectronic aluminum). Examples of such interactions are the $2p^5 3s^2 3p3d + 2p^5 3s 3p3d^2$ mixing and the perturbing effect of the $2p^5 3s 3p^3$configuration. These CI effects are also predicted to be stronger in the Si^+ ion than in the aluminum atom [38,57].

In Fig. 5 (middle panel) the calculated MCDF energy values were increased by 1.3 eV to bring the strong resonances at ∼111 eV into coincidence with the experimental values. Apart from this constant shift, the overall agreement between the experimental and MCDF cross sections is quite good. In particular, below 112 eV the relative positions (to one another)

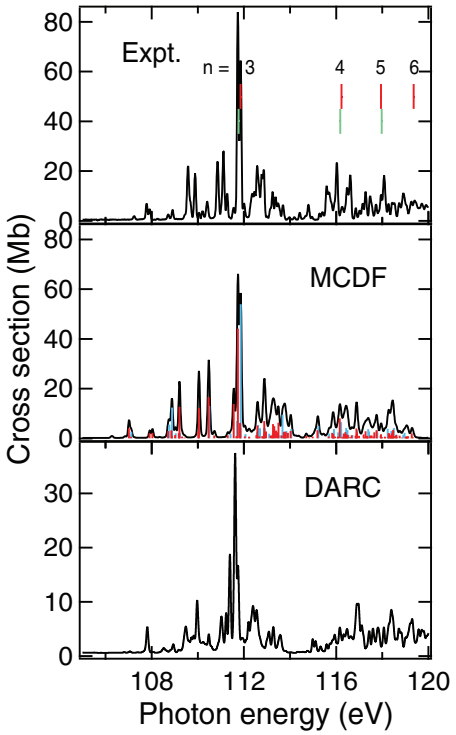

FIG. 5. (Color online) Variation of the photoionization cross section for the Si^+ ion in the 105–120 photon energy range. The top panel shows the experimental cross section obtained from the sum of the single- and double-PI cross sections shown in Fig. 4. The middle panel shows the MCDF theoretical cross section (black curve). The heights of the sticks give the relative contribution of the Si^+ $3s^2 3p^2 P$ ground levels with $J = 1/2$ and $3/2$ shown in blue (light gray) and red (dark gray), respectively. A constant shift of 1.3 eV has been added to the *ab initio* energy values (see the text). The bottom panel shows the theoretical DARC cross section. Both theoretical cross sections have been reconstructed assuming a 10% population of the ions in the ^4P metastable levels and convolution by a Gaussian profile with 80-meV FWHM (see the text).

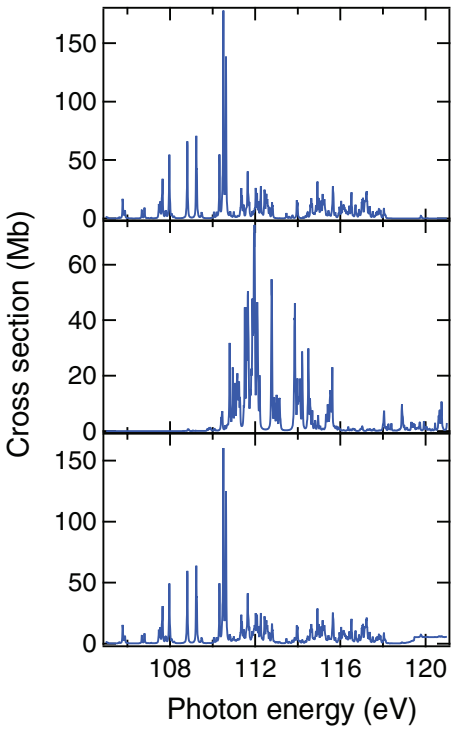

FIG. 6. (Color online) The MCDF calculated single-PI cross section of the Si^+ ion in the 105–120 eV photon energy range. The top panel shows the calculated cross section assuming 100% ground configuration ^2P population. The middle panel shows the calculated cross section assuming 100% ^4P metastable-state population. The bottom panel shows the reconstructed calculated cross section assuming 90% ground-state and 10% metastable-state populations of the ions (see the text).

and relative strengths of the observed resonances seem well reproduced by the calculations.

From Table III we see that up to ∼111-eV photon energy, almost all the $2p$ excited resonances decay predominantly in the single-ionization channel with typical single- to double-ionization ratios of ∼0.97/0.03. This is readily explained in terms of the resonant Auger processes discussed above. In the 111–112 eV range (resonances labeled 17–26), this ratio can be as low as 1.3 (resonance 17 at 111.037 eV) and typically lies between 3 and 6. Therefore, the decay of the corresponding $2p$ excited states has seen a sharp increase in the probability of shake-off processes leading to the ejection of a second electron. These are attributable to strong correlation (CI) effects in the electron configurations involved. Table III shows the *ab initio* values of the MCDF calculated energies, which differ from the experimental values, by up to 2 eV in some cases. Nevertheless, the relative energy differences and strengths of the MCDF calculated resonances, compared to the experimental data, enabled us to make the assignments listed in Table III. In Fig. 5 the energy of the strong $2p\,^2P \rightarrow 3d\,^2D$ resonance resulting from the DARC calculations is seen to be in good agreement with the experimental value. However, the detailed agreement of the other resonance structures with experiment, as predicted by the DARC calculations, is not as good as for the MCDF results. The relative strengths of the resonances below about 111 eV are better reproduced by the MCDF calculations and the absolute cross-section values are in good agreement with experiment. Above the 111-eV resonance the overall shape of the cross-section behavior is well reproduced by the DARC approximation, but the overall absolute cross-section values are under estimated.

Numerous resonances were measured in the 112–120 eV range, i.e., up to the $2p^5 3s^2 3p$ thresholds (shown in Fig. 1). Their peak energy positions, oscillator strengths (f value), and single- to double-ionization ratios are shown in Table V. Due to the large energy overlaps of the individual resonances advancing closer to the $2p$ ionization limits, the relative errors on the f values in Table V are significantly larger (upward of 20%) than in Table III. The resonances in this region are associated with higher-lying *LSJ* states built on the $2p^5 3s^2 3pnd$, $n \geqslant 3$; $2p^5 3s^2 3pns$, $n \geqslant 4$; and $2p^5 3s 3p^2 np$, $n \geqslant 3$ configurations; these states show almost complete mixing, rendering single spectral assignments virtually meaningless. According to the MCDF calculations, the prominent resonances marked in Fig. 5 at 117.268, 118.073, and 118.901 eV are associated with $4d(^3P)^2D_{3/2,5/2}$, $5d(^3P)^2D_{3/2,5/2}$, and $6d(^3P)^2D_{3/2,5/2}$ Rydberg states, respectively, and show roughly equal decay strengths

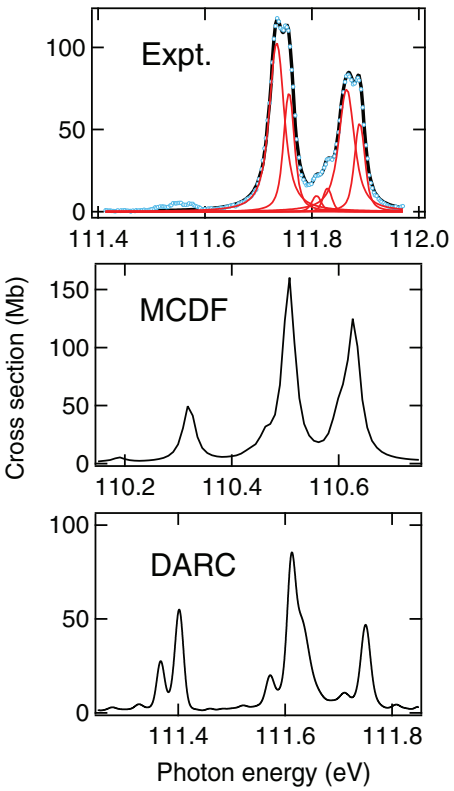

FIG. 7. (Color online) Single-PI cross section measured in the 111.4–112 eV photon energy range with 16-meV BP (open points). It was fitted (black curve) by six individual Voigt profiles shown by the red (dark gray) curves. The corresponding MCDF and DARC theoretical simulations are shown in the middle and bottom panels, respectively.

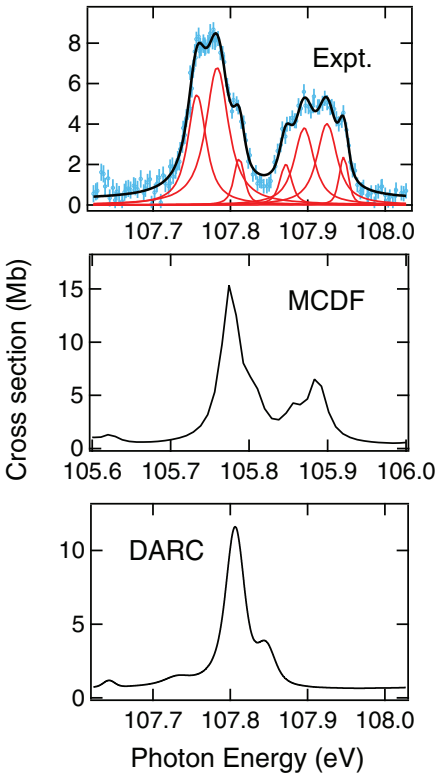

FIG. 8. (Color online) The top panel shows the single-PI cross sections, measured with 16-meV BP, in the 107.6–108.1 eV photon energy range shown by blue (light gray) points with an error bar representing the statistical uncertainty. It was fitted (black curve) by seven individual Voigt profiles of fixed 16-meV Gaussian widths shown by the red (dark gray) curves. The corresponding MCDF and DARC theoretical simulations are shown in the middle and bottom panels, respectively.

in the single- and double-ionization channels. Generally, the experimental data in Table V show a significant and almost continuous increase in the double-ionization signal from ∼116 eV. Between 116 and 118 eV this can be explained by the existence of doubly excited intermediate states of Si^{2+} of the type $2p^5 3s 3p^2$ or $2p^5 3s 3d^2$, which provide an additional pathway for a sequential decay to the Si^{3+} ion, therefore appearing in the doubly ionized channel. Further pathways open up for Rydberg states lying above the photon energies associated with the $2p$ inner thresholds, beginning at about 118 eV (marked by vertical bars in Fig. 1). The contributions of the two processes explain the observed increase in the double-photoionization channel.

In the above we have discussed the general overall agreement between the relative cross sections as measured compared to the calculations. The experimental cross sections are, however, on an absolute scale (see Sec. II). In order to compare the calculations with the absolute measurements we have calculated the sum of the cross sections between 105 and 120 eV for the experimental data and for the MCDF and DARC calculations. The results for the integrated cross sections (from Fig. 5) are 80.1 Mb eV for experiment, 83.2 Mb eV for MCDF calculations, and 45.1 Mb eV for the DARC calculations. Taking into account the experimental uncertainty of ∼15%, it is seen that while the MCDF absolute cross section agrees well with experiment, the value calculated from the DARC again underestimates the cross section, indicating the importance of experiments for benchmarking.

In order to further test the MCDF and DARC theoretical predictions against the experimental data, we also carried out higher-resolution scans with a 16-meV bandpass in two narrow photon regions 111.4–112.0 and 107.6–108.1 eV, presented in Figs. 7 and 8, respectively. In both figures the blue (light gray) points represent the measured single-photoionization cross sections with statistical error bars. The red (dark gray) curves are the results of the unconstrained fitting of the experimental points using Voigt profiles of fixed Gaussian width equal to 16 meV, with the Lorentzian width, peak energy positions, and intensities as the fitting parameters. The black curves in each figure are the sum of the underlying Voigt profiles and represent the best fits to the experimental data. Detailed comparisons of the theoretical MCDF and DARC resonance energies and widths can be made with those extracted from the measured profiles as just explained. The fitted peak energies and f values are represented in Table IV. For the 111.4–112.0 eV resonances, Table IV also lists the Lorentzian widths extracted for the fitted resonances. These are not included for the 107.6–108.1 eV resonances because the lower signal-to-noise ratio in the experimental spectral profiles makes the extracted Lorentzian widths unreliable. The middle and bottom panels

TABLE IV. Energy positions, oscillator strengths (f value), and Lorentzian linewidths of the fine-structure components (obtained from computational fits of multiple Voigt profiles) of selected resonances measured with high-energy resolution (16-meV bandpass) in the single-photoionization cross section of Si^+. The relative energy uncertainties in meV are shown in parentheses in column 2 and the absolute uncertainties in the widths are shown in parentheses in column 4. The uncertainty on the f value does not include the contribution of the systematic uncertainties.

Resonance label	Fitted peak energy (eV)	f value (error in %)	Width (meV)
3*a*	107.757	1.9×10^{-3}(32)	
3*b*	107.784(2)	2.7×10^{-3}(36)	
3*c*	107.812(2)	3.9×10^{-4}(62)	
4*a*	107.870(3)	3.0×10^{-4}(115)	
4*b*	107.895(3)	1.6×10^{-3}(74)	
4*c*	107.925(3)	1.3×10^{-3}(85)	
4*d*	107.946(3)	3.8×10^{-4}(86)	
22*a*	111.515	4.7×10^{-4}(43)	11(7)
22*b*	111.546(4)	1.3×10^{-3}(29)	18(6)
22*c*	111.574(4)	1.0×10^{-3}(31)	16(5)
23*a*	111.734(4)	4.0×10^{-2}(13)	25(1)
23*b*	111.757(4)	1.9×10^{-2}(13)	13(1)
24*a*	111.808(4)	2.1×10^{-3}(18)	9(2)
24*b*	111.829(4)	2.8×10^{-3}(20)	6(2)
25*a*	111.865(4)	3.1×10^{-2}(13)	27(1)
25*b*	111.889(4)	1.3×10^{-2}(14)	12(1)

of Figs. 7 and 8 also show the theoretical profiles predicted in the same energy region by the MCDF and DARC theories, respectively. The differences between the results of the two calculations and between theory and experiment show that while theory can produce reasonable overall agreement with the general energy-dependent behavior (Fig. 5) of the cross section, this agreement breaks down when looked at in detail. This is not too surprising due to the complexity of the atomic problem associated with the many open shells referred to earlier. It should be noted that while ions in the ^4P metastable states play a minor role in the 111–112 eV region, this is not the case for the 107–108 eV resonances.

C. Photoionization cross section between 120 and 137 eV

The variations of the photoionization cross section measured in the double-ionization channel are shown in Fig. 9 as a function of the photon energy in the 119–138 eV range. Above the onset, the synchrotron photon can directly ionize a $2p$ -subshell electron, producing a Si^{2+} ion in the $2p^5 3s^2 3p$ configuration (magnesium isolectronic sequence), which will subsequently Auger decay primarily to $2p^6 3s$ or $2p^6 3p$ in Si^{3+}. This will appear as an energy continuous process in the double-photoionization channel and this is compatible with the behavior observed in Fig. 9. The absolute cross-section measurements indicate an almost constant value around 5 Mb from the onset to the limit of our observations at 137-eV photon energy. These are in very good agreement with the MCDF theoretical and the semiempirical continuous cross sections [58] also shown in the figure. We note that this agreement further

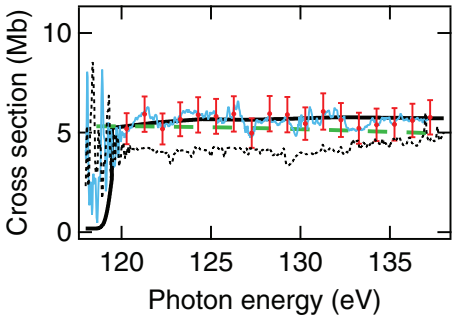

FIG. 9. (Color online) Variations of the double-PI cross section in the 118–138 eV photon energy range. The blue (light gray) curve shows the experimental cross sections measured in the relative mode while the red (dark gray) data points are the absolute measurements. The solid black line, dotted line, and dashed line show the MCDF direct PI cross section, DARC theoretical results, and cross sections from Verner *et al.* [58], respectively.

justifies our choice of the MCDF calculations in determining the metastable fraction in Sec. IV A.

Discrete resonance structures are also discernible superimposed on the continuous cross section. A window appears near 122.5 eV, which may correspond with the decay of high-lying doubly excited configurations of the type already discussed, e.g., $2p^5 3s 3p^2 4p$; more extensive calculations would be needed to ascertain this point. However, a comparison with the double-photoionization cross section in Si^{2+} [33] suggests that this is probably the correct assignment. An asymmetric Fano-type resonance distinctly appears near 126.5 eV. Again, by reference to the previous work in Si^{2+}, this resonance can be assigned with reasonable certainty to the excitation of a $2s$ -subshell electron leading to $2s 2p^6 3s 3p^2$ photoexcited states. None of the calculated cross sections presented in this work include $2s \rightarrow np_{1/2,3/2}$ excitations.

It is notable that the DARC results, also shown in Fig. 9, underestimate the absolute value of the above-threshold cross section. This mirrors the underestimate of the cross section in the 104–120 eV region. The DARC calculations, however, show clearly the growth in strength of doubly excited resonances close to the threshold and also indicate doubly excited structures above the threshold, similar to those obtained in the experimental data.

While Tables II and V show the relative importance of single ionization (SI) versus double ionization (DI) as a function of the photon energy, the magnitude of the much weaker triple ionization (TI) was measured at only two photon energies, 118.9 eV corresponding to a resonance and 121 eV in the continuum region (see Fig. 9). Assuming the form factor [see Eq. (1)] was constant during the consecutive measurements of DI and TI, the corresponding values are 118.9 eV, with a SI of 3.4 Mb, DI of 8.2 Mb, and TI of 0.004(4) Mb, and 121 eV with a SI of 0.3 Mb, DI of ∼6 Mb, and TI of 0.09(1) Mb.

V. CONCLUSION

We have measured the absolute photoionization cross section of aluminumlike Si^+ ion in the 94–137 eV photon energy range. The measurements were performed using the

TABLE V. Measured energy position, oscillator strength (f value), and single- to double-ionization ratio, spectral assignments, and theoretical MCDF energy of $2p$ -subshell excited resonances in the single- and double-photoionization cross sections of Si^+ in the 112–120 eV photon energy range. The relative energy uncertainties in meV are shown in parentheses in column 2.

Resonance label	Measured energy (eV)	Measured f value (% error)	Single- to double-ionization ratio
27	112.180(12)	4.9×10^{-4}(50)	0/100
28	112.288(6)	3.2×10^{-3}(51)	83/17
29	112.364(3)	1.2×10^{-2}(30)	88/12
30	112.462(2)	8.0×10^{-3}(22)	94/6
31	112.569(2)	1.8×10^{-2}(19)	95/5
32	112.647(3)	1.3×10^{-2}(19)	94/6
33	112.765(2)	1.6×10^{-2}(16)	85/15
34	112.858(2)	1.7×10^{-2}(13)	92/8
35	113.004(3)	1.2×10^{-3}(25)	97/3
36	113.139(2)	4.3×10^{-3}(20)	89/11
37	113.242(2)	1.0×10^{-2}(20)	95/5
38	113.370(3)	9.0×10^{-3}(18)	93/7
39	113.482(4)	6.9×10^{-3}(36)	95/5
40	113.553(8)	2.3×10^{-3}(52)	85/15
41	113.692(2)	6.6×10^{-3}(21)	89/11
42	113.963(3)	1.1×10^{-3}(17)	100/0
43	114.186(2)	8.1×10^{-4}(17)	100/0
44	114.418(2)	2.5×10^{-3}(19)	90/10
45	114.673(4)	2.3×10^{-3}(16)	100/0
46	114.798(2)	6.5×10^{-3}(17)	94/6
47	114.956(2)	8.0×10^{-4}(16)	100/0
48	115.276(3)	1.8×10^{-3}(20)	38/62
49	115.411(2)	3.7×10^{-3}(15)	58/42
50	115.578(2)	1.3×10^{-2}(14)	67/33
51	115.689(2)	1.6×10^{-2}(15)	79/21
52	115.799(2)	5.4×10^{-3}(17)	100/0
53	115.921(2)	3.6×10^{-3}(16)	100/0
54	116.028(2)	2.9×10^{-2}(13)	82/18
55	116.255(2)	9.0×10^{-3}(19)	90/10
56	116.48(2)	2.3×10^{-2}(16)	89/11
57	116.614(2)	1.6×10^{-2}(17)	89/11
58	116.849(2)	4.1×10^{-3}(25)	8020
59	117.012(2)	3.7×10^{-3}(23)	78/22
60	117.136(2)	5.9×10^{-3}(23)	52/48
61	117.268(2)	1.3×10^{-2}(21)	57/43
62	117.462(2)	6.5×10^{-3}(29)	68/32
63	117.533(3)	6.9×10^{-3}(34)	61/32
64	117.719(2)	6.2×10^{-3}(42)	52/48
65	117.834(4)	1.7×10^{-3}(67)	34/66
66	117.932(2)	8.1×10^{-3}(41)	40/60
67	118.073(2)	2.6×10^{-2}(29)	58/42
68	118.272(2)	5.1×10^{-3}(35)	62/38
69	118.421(3)	5.9×10^{-3}(34)	56/44
70	118.52(2)	8.3×10^{-3}(36)	60/40
71	118.726(2)	5.5×10^{-3}(94)	66/34
72	118.901(3)	2.8×10^{-2}(134)	39/61
73	119.058(6)	2.9×10^{-3}(218)	0/100
74	119.232(2)	6.7×10^{-3}(200)	15/85
75	119.402(3)	2.7×10^{-2}(152)	39/61
76	119.682(4)	1.4×10^{-2}(179)	25/75
77	119.924(6)	1.2×10^{-2}(215)	0/100

MAIA merged-beam setup on the PLEIADES beamline of the SOLEIL synchrotron radiation facility. Signals in both the Si^{2+} and Si^{3+} photoionization channels, produced from the $2p$ subshell of Si^+ ions from the two levels ($^2P_{1/2,3/2}$) of the ground configuration $1s^2 2s^2 2p^6 3s^2 3p$ and the metastable levels ($^4P_{1/2,3/2,5/2}$) of the configuration

$1s^2 2s^2 2p^6 3s 3p^2$, were observed. The experimental data are compared with the results of MCDF- and DARC-based calculations. While the overall comparisons are reasonable, nevertheless, significant differences are seen between the two calculations and between both with experiment. The results show the continuing importance of experiments to benchmark different photoionization cross-section calculations.

ACKNOWLEDGMENTS

We would like to thank the SOLEIL staff and in particular C. Nicolas, the local contact for the PLEIADES beamline. B.M.M. acknowledges support from the U.S. National Science Foundation through a grant to ITAMP at the Harvard-Smithsonian Center for Astrophysics under the visitors program, the RTRA network Triangle de la Physique, and a visiting research fellowship from Queen's University Belfast. This research used computational resources of the National Energy Research Scientific Computing Center in Oakland, CA, USA and at the High Performance Computing Center Stuttgart of the University of Stuttgart, Stuttgart, Germany. J.P.M., P.V.K., and E.T.K. would like to acknowledge the financial support from Calipso, Wayforlight (www.calipso.wayforlight.eu). Calipso is a project funded by the European Commission under the 7th Framework programme to facilitate transnational access to European synchrotron and free electron laser facilities.

[1] D. W. Savin, N. S. Brickhouse, J. J. Cowan, R. P. Drake, S. R. Federman, G. J. Ferland, A. Frank, M. S. Gudipati, W. C. Haxton, E. Herbst, S. Profumo, F. Salama, L. M. Ziurys, and E. G. Zweibel, Rep. Prog. Phys. **75**, 036901 (2012).
[2] J. N. Bregman and J. P. Harrington, Astrophys. J. **309**, 833 (1986).
[3] D. W. Savin and J. M. Laming, Astrophys. J. **566**, 1166 (2002).
[4] A. R. Foster, R. K. Smith, N. S. Brickhouse, T. R. Kallman, and M. C. Witthoeft, Space Sci. Rev. **157**, 135 (2010).
[5] P. Quinet, P. Palmeri, C. Mendoza, M. A. Bautista, J. Garcia, M. C. Witthoeft, and T. R. Kallman, J. Electron Spectrosc. Relat. Phenom. **184**, 170 (2011).
[6] A. R. Foster, R. K. Smith, and N. S. Brickhouse, Astrophys. J. **756**, 128 (2012).
[7] M. A. Bautista, V. Fivet, P. Quinet, J. Dunn, T. R. Gull, T. R. Kallman, and C. Mendoza, Astrophys. J. **770**, 15 (2013).
[8] R. Kisielius, V. P. Kulkarni, G. J. Ferland, P. Bogdanovich, and M. L. Lykins, Astrophys. J. **780**, 76 (2014).
[9] F. Paerels, J. Cottam, M. Sako, D. A. Liedahl, A. C. Brinkman, R. L. J. van der Meer, J. C. Kaarstra, and P. Predehl, Astrophys. J. **533**, L135 (2000).
[10] D. G. J. Sutherland, G. M. Bancroft, J. D. Bozek, and K. H. Tan, Chem. Phys. Lett. **199**, 341 (1992).
[11] R. Puttner, M. Domke, D. Lentz, and G Kaindl, Phys. Rev. A **56**, 1228 (1997).
[12] S. Wlodek and D. K. Bohme, J. Am. Chem. Soc. **111**, 61 (1989).
[13] S. G. Sayres, M. W. Ross, and A. W. Castleman, Jr., Phys. Rev. A **82**, 033424 (2010).
[14] T. Lanz, M.-C. Artru, M. Le Dourneuf, and L. Hubeny, Astron. Astrophys. **309**, 218 (1996).
[15] T. Lanz and M.-C. Artru, Phys. Scripta **32**, 115 (1985).
[16] M.-C. Artru and T. Lanz, Astron. Astrophys. **182**, 273 (1987).
[17] S. N. Nahar and A. K. Pradhan, Astrophys. J. **447**, 966 (1995).
[18] J. C. Weisheit, Astrophys. J. **190**, 735 (1974).
[19] A. G. Kochur, D. Petrini, and E. P. Silva, Astron. Astrophys. **393**, 1081 (2002).
[20] E. T. Kennedy, J. T. Costello, J.-P. Mosnier, A. A. Cafolla, M. Collins, L. Kiernan, U. Koeble, M. H. Sayyad, and M. Shaw, Opt. Eng. **33**, 3984 (1994).
[21] E. T. Kennedy, J. T. Costello, A. Gray, C. McGuinness, J.-P. Mosnier, and P. van Kampen, J. Electron Spectrosc. Relat. Phenom. **101-103**, 161 (1999).
[22] C. McGuinness, M. Martins, Ph. Wernet, B. F. Sonntag, P. van Kampen, J.-P. Mosnier, E. T. Kennedy, and J. T. Costello, J. Phys. B **32**, L583 (1999).
[23] H. Kjeldsen, J. Phys. B **39**, R325 (2006).
[24] M. F. Gharaibeh, N. El Hassen, M. M. Al Shorman, J.-M. Bizau, D. Cubayne, S. Guilbaud, I. Sako, C. Blancard, and B. McLaughlin, J. Phys. B **47**, 065201 (2014).
[25] D. Kilbane, F. Folkmann, J.-M. Bizau, C. Banahan, S. Scully, H. Kjeldsen, P. van Kampen, M. W. D. Mansfield, J. T. Costello, and J. B. West, Phys. Rev. A **75**, 032711 (2007).
[26] M. F. Gharaibeh, A. Aguilar, A. M. Covington, E. D. Emmons, S. W. J. Scully, R. A. Phaneuf, A. Müller, J. D. Bozek, A. L. D. Kilcoyne, A. S. Schlachter, I. Àlvarez, C. Cisneros, and G. Hinojosa, Phys. Rev. A **83**, 043412 (2011).
[27] T. R. Kallman, Rev. Mod. Phys. **79**, 79 (2007).
[28] G. J. Ferland, R. L. Porter, P. A. M. van Hoof, R. J. R. Williams, N. P. Abel, M. L. Lykins, G. Shaw, W. J. Henney, and P. C. Stancil, Rev. Mex. Astron. Astr. **49**, 137 (2013).
[29] E. T. Kennedy, J. T. Costello, and J.-P. Mosnier, J. Electron Spectrosc. Relat. Phenom. **79**, 283 (1996).
[30] C. Blancard, Ph. Cosse, G. Faussurier, J.-M. Bizau, D. Cubaynes, N. El Hassan, S. Guilbaud, M. M. Al Shorman, E. Robert, X.-J. Liu, C. Nicolas, and C. Miron, Phys. Rev. A **85**, 043408 (2012).
[31] M. H. Sayyad, E. T. Kennedy, L. Kiernan, J-P. Mosnier, and J. T. Costello, J. Phys. B **28**, 1715 (1995).
[32] H. S. Chakraborty, A. Gray, J. T. Costello, P. C. Deshmukh, G. N. Haque, E. T. Kennedy, S. T. Manson, and J.-P. Mosnier, Phys. Rev. Lett. **83**, 2151 (1999).
[33] J.-P. Mosnier, M. H. Sayyad, E. T. Kennedy, J.-M. Bizau, D. Cubaynes, F. J. Wuilleumier, J.-P. Champeaux, C. Blancard, R. H. Varma, T. Banerjee, P. C. Deshmukh, and S. T. Manson, Phys. Rev. A **68**, 052712 (2003).
[34] J.-M. Bizau, J.-P. Mosnier, E. T. Kennedy, D. Cubaynes, F. J. Wuilleumier, C. Blancard, J.-P. Champeaux, and F. Folkmann, Phys. Rev. A **79**, 033407 (2009).
[35] M. F. Gharaibeh, J. M. Bizau, D. Cubaynes, S. Guilbaud, N. El Hassan, M. M. Al Shorman, C. Miron, C. Nicolas, E. Robert,

C. Blancard, and B. M. McLaughlin, J. Phys. B **44**, 175208 (2011).
[36] A. Lindblad, J. Soderstorm, C. Nicolas, E. Robert, and C. Miron, Rev. Sci. Instrum. **84**, 113105 (2013).
[37] J. T. Costello, E. T. Kennedy, J.-P. Mosnier, M. H. Sayyad, and C. McGuinness, J. Phys. B **31**, L547 (1998).
[38] J. T. Costello, E. T. Kennedy, J.-P. Mosnier, and M. H. Sayyad, J. Phys. B **31**, 677 (1998).
[39] J. A. R. Samson, *Techniques of Vacuum Ultraviolet Spectroscopy* (Wiley, New York, 1967).
[40] C. G. King, M. Tronc, F. Read, and R. C. Bradford, J. Phys. B **10**, 2479 (1977).
[41] H. Kjeldsen, F. Folkmann, J. van Elp, H. Knudsen, J. B. West, and T. Andersen, Nucl. Instrum. Methods Phys. Res. Sect. B **234**, 349 (2005).
[42] B. M. McLaughlin, J. M. Bizau, D. Cubaynes, M. M. Al Shorman, S. Guilbaud, I. Sakho, C Blancard, and M. F. Gharaibeh, J. Phys. B **47**, 115201 (2014).
[43] J. Bruneau, J. Phys. B **17**, 3009 (1984).
[44] C. P. Ballance and D. C. Griffin, J. Phys. B **39**, 3617 (2006).
[45] P. H. Norrington and I. P. Grant, J. Phys. B **20**, 4869 (1987).
[46] W. P. Wijesundera, F. A. Parpia, I. P. Grant, and P. H. Norrington, J. Phys. B **24**, 1803 (1991).
[47] P. H. Norrington, DARC codes, http://web.am.qub.ac.uk/DARC
[48] V. Fivet, M. A. Bautista, and C. P. Ballance, J. Phys. B **45**, 035201 (2012).
[49] B. M. McLaughlin and C. P. Ballance, J. Phys. B **45**, 095202 (2012).
[50] B. M. McLaughlin and C. P. Ballance, J. Phys. B **45**, 085701 (2012).
[51] G. Hinojosa, A. M. Covington, G. A. Alna'Washi, M. Lu, R. A. Phaneuf, M. M. Sant'Anna, C. Cisneros, I. Álvarez, A. Aguilar, A. L. D. Kilcoyne, A. S. Schlachter, C. P. Ballance, and B. M. McLaughlin, Phys. Rev. A **86**, 063402 (2012).
[52] K. G. Dyall, I. P. Grant, C. T. Johnson, and E. P. Plummer, Comput. Phys. Commun. **55**, 425 (1989).
[53] F. Parpia, C. Froese Fischer, and I. P. Grant, Comput. Phys. Commun. **94**, 249 (1996).
[54] I. P. Grant, *Quantum Theory of Atoms and Molecules: Theory and Computation* (Springer, New York, 2007).
[55] Y. Ralchenko, A. E. Kramida, J. Reader, and NIST ASD Team, NIST Atomic Spectra Database, version 4.0.1 (National Institute of Standards and Technology, Gaithersburg, 2011), available at http://physics.nist.gov/asd3
[56] J. P. Mosnier, J. T. Costello, E. T. Kennedy, L. Kiernan, and M. H. Sayyad, Phys. Rev. A **49**, 755 (1994).
[57] K. Jankala, S. Fritzsche, M. Huttula, J. Schulz, S. Urpelainen, S. Heinasmaki, S. Aksela, and H. Aksela, J. Phys. B **40**, 3435 (2007).
[58] D. H. Verner, D. G. Yakovlev, I. M. Band, and M. B. Trzhaskovskaya, At. Data Nucl. Data Tables **55**, 233 (1993).